Discrete Element Modelling of Methane Hydrate Soil Sediments using Elongated Soil Particles

Yanxin Yu [a, 1] (yanxin.yu.10@alumni.ucl.ac.uk)

Yi Pik Cheng [a] (yi.cheng@ucl.ac.uk)

Xiaomin Xu [b] (xuxiaominzju@gmail.com)

Kenichi Soga [b] (ks207@cam.ac.uk)

a. Civil, Environmental and Geomatic Engineering, Chadwick Building, University College London, Gower Street, London, WC1E 6BT, United Kingdom

b. Geotechnical and Environmental Research Group, Department of Engineering, University of Cambridge, Trumpington Street, Cambridge, CB2 1PZ, United Kingdom

---

* Corresponding author: Yanxin Yu (yanxin.yu.10@alumni.ucl.ac.uk)

Present address: 1. China Oil And Gas Group Limited, Suite 2805, 28/F., Sino Plaza, 255-257 Gloucester Road, Causeway Bay, Hong Kong

---

Abstract

In this Discrete Element Modelling research, triaxial compression tests of particle assemblies were simulated to study the mechanical behaviour of methane hydrate sediments with two different hydrate formation patterns: pore-filling and cementation. The soil particles were modelled using spherical or elongated particles (two aspect ratios 1.5 and 2.0). Hydrates were modelled as smaller particles and were placed either inside the pores in a random manner (the pore-filling case) or around the soil particle contacts (the cementation case). Compared to the pure soil samples, the hydrates essentially influenced the mechanical behaviour of the hydrate-bearing soil samples, and the behaviours varied due to the different hydrate growth patterns. The behaviour with elongated soil particles is much closer to that of the natural hydrate-bearing sandy sediments retrieved from the Nankai Trough than the behaviour with spherical particles. The observed macroscopic strength behaviour is also explained by the microscopic contact-type related contributions (soil-soil contact, soil-hydrate contact and hydrate-hydrate contact) to the deviatoric stresses.

Keywords

Methane hydrate, Soil, DEM, Saturation, Particle shape, Anisotropy

1. Introduction

Methane hydrate develops and exists in the pores of soil sediments under deep seabeds or permafrost regions under conditions of low temperature and high pressure. The investigation on the geomechanical behaviour of methane hydrate bearing soils has attracted increasing interest, as methane gas is a potential energy source that can be extracted by dissociating the hydrates in-situ from the hydrate-bearing sediments [1, 2].

Among all the known hydrate distribution patterns, the most typical patterns considered for coarse grained hydrate bearing sediments are the pore-filling and the cementation patterns, as shown in Fig. 1. In the pore-filling pattern, hydrates freely grow in the pores without connecting two or more soil particles together [1, 3]. On the other hand, in the cementation case, hydrates nucleate at inter-granular contacts along the soil particle surface. The existing soil skeleton structure is bonded by the hydrates, whilst the soil-soil contacts are not bonded [1, 4]. In both patterns, the soil skeleton, which has been formed by consolidation under high pressure, is not broken by the growth of hydrates inside the pores.

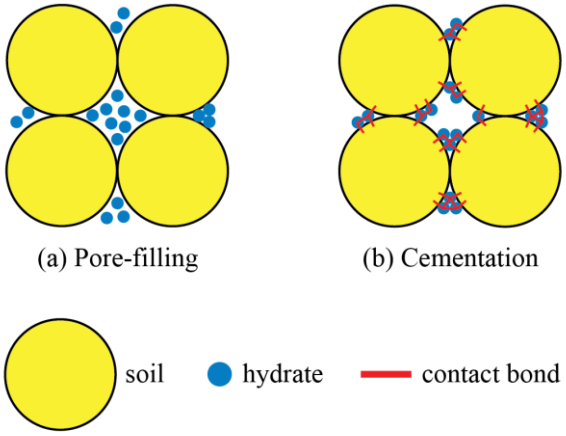

Fig. 1. Pore-scale hydrate distribution patterns of hydrate-bearing sediments: (a) pore-filling, (b) cementation

The mechanical behaviour of hydrate-bearing soil sediments is dependent on the hydrate growth pattern, hydrate morphology and hydrate saturation [5-12]. For example, two hydrate formation patterns were prepared by Masui et al. [12]: the strong bond sample (cementation pattern) and the weak bond sample (considered as the pore-filling pattern). Toyoura sand was used as the sediment sand. In both cases, with stiffness at 50% stress level (E_{50}), peak strength (maximum deviator stress) and dilation angle at peak strength increased with hydrate saturation; however, the hydrate samples with the cementation pattern indicated a greater effect of hydrate than the hydrate samples with the pore filling pattern.

In this paper, the Discrete Element Method (DEM) was used to study the mechanical behaviour of the hydrate-bearing soil with different growth patterns. DEM allows to model of the granular materials by explicitly considering their true particulate nature [13]. Two typical types of microscopic hydrate distribution patterns inside soil pores were modelled: (*i*) pore-filling and (*ii*) cementation (see Fig. 1), using the discrete element code Particle Flow Code Three Dimensions Version 4.0 (PFC^{3D} 4.0) [14]. In the pore-filling model [15-17], hydrates nucleate on sediment grain boundaries and grow freely into pore spaces without bridging two or more particles together. In the cementation model [17, 18], hydrates nucleate at inter-granular contacts and the existing soil skeleton structure is cemented by the hydrates, while the soil-soil (s-s) contacts are not bonded. In most of the previous DEM studies simulating the behaviour of methane hydrate soils [15-20], it was assumed that all the soil and hydrate particles were spheres. However, it is well known that the shape of soil particles has a large influence on its mechanical behaviour [17, 21, 22]. In this study, elongated soil particles were used to

investigate the stress-strain and volumetric responses by performing a series of DEM drained triaxial compression tests, and to make a comparison between the pore-filling and cementation models with both spherical and elongated soil particles. A microstructure study of contact-type related contributions to the deviatoric stresses was conducted to gain insights into the mechanical behaviour during the deformation process.

2 DEM Sample Preparation

Due to the computational limitation, the initial size of the cylindrical samples was set to 3.5 mm in height and 1.75 mm in diameter, with an aspect ratio of 2. The soil sample was initially prepared by generating 2,000 sphere particles with diameters ranging from 0.1mm to 0.25mm (following Gaussian distribution) in a cylindrical region with rigid frictionless walls. This size range followed that of Masui *et al* [12], although the sample size was much smaller than a typical triaxial sample. During this assembly generation stage, the initial value of porosity and inter-particle friction are set to 0.43 and 0.75, respectively. The radius expansion method was adopted to facilitate the creation of this initial porosity during the initial sample preparation state at zero confinement. Once the DEM assembly has been generated, a numerical servo-control mechanism was activated to compress the specimen to reach a desired isotropic stress state (e.g. 1 MPa, 2 MPa and 3 MPa in this study).

Considering the development of natural hydrate bearing sediments in very deep underground, it is assumed that hydrates are formed after the geostatic stresses are carried by the soil skeleton. Hydrate particles were randomly generated in the void space of the consolidated soil sample, until it reaches the desired hydrate saturation (S_h). Fig. 2 shows an example of the sample preparation

process of the pore filling case. In this study, the case of S_h = 40% was the maximum number of hydrate particles that could be created in the void space without breaking the soil skeleton. The total number of soil and hydrate particles was more than 40,000 with a saturation of 40%. Note that the hydrate saturation ratios reported in this study is a lower bound approximation, due to geometric nature of the aggregates of the hydrate spheres (i.e. pores created within the aggregates). It could be easily extrapolated to a higher saturation of the natural hydrate bearing soil sediments [18].

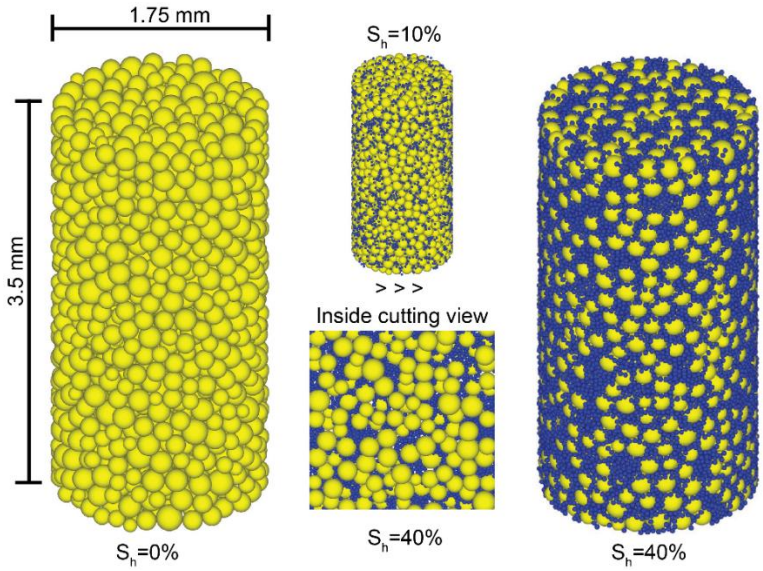

Fig. 2. DEM hydrate-bearing soil samples

In order to achieve a uniform distribution of the hydrate particles in the cementation case, six directions of gravitational forces were applied in stages. For a given saturation, the desired amount of hydrate particles was evenly divided into six groups. Each of them was then assigned with a certain direction of gravity. Hydrate particles then dropped along the gravity direction until they stopped at the soil-soil contacts, and then gradually accumulated along the soil particle surfaces. It was checked to ensure that each hydrate particle had made at least two contacts with either soil particles or other hydrate particles [17, 18]. Once the system reached an overall equilibrium state, all these hydrate-soil and

hydrate-hydrate contacts were then be bonded. The process was repeated for the next group of hydrate particles with a different gravity direction. Note that the soil skeleton was carefully kept undisturbed during this whole process using a special subroutine in written in the FISH commands of PFC3D.

The parameters for the DEM simulations are listed in Table 1. For example, the elastic modulus of 286 MPa was chosen for the soil particles [23, 24]. In this study, the selection of Young's modulus (E) for hydrate particle is based on the hydrate-soil elastic modulus ratio, which is defined as the ratio between the Young's modulus of hydrate particle and that of soil particle. Brugada et al. (2010) had performed a parametric study on this issue, and concluded that the value of 0.1 is suitable for modelling the mechanical behaviour of methane hydrate. Similar or even lower ratio has also been used in other references, depending on the contact model used [27]. The normal contact stiffness k_n was set to be proportional to the particle elastic modulus (E_c) and the particle diameter (D). The bonding strength was determined such that the cementation effect was apparent but not too strong [17, 25].

Property	**Soil**	**Methane hydrate**
Particle size D (mm) (Gaussian distribution)	0.1-0.25	0.04
Density ρ (kg/m^3)	2600	900
Elastic Modulus E_c (MPa)	286	28.6
Normal contact stiffness k_n (N/m)	$2DE_c$	$2DE_c$
Shear contact stiffness k_s (N/m)	$0.7k_n$	$0.7k_n$
Inter-particle friction μ	0.75	0.75

Bonding strength, B_n=B_s (N)	$5x10^3$

Table 1: Input parameters used in the DEM model

To examine the particle shape effect, each spherical soil particle inside the consolidated specimen were replaced by elongated clump particles with the same volume. As shown in Fig. 3, two aspect ratios were chosen for the elongated particles: 1.5 (2-ball clump) and 2.0 (3-ball clump). Note that the replacement of soil particles would alter the original soil fabric. In order to minimize this effect, the replacement process of all soil particles was performed one after another, rather than all at once. There was also a certain time interval between each sub-replacement, to allow the updated system maintaining equilibrium with a minimized disturbance. By doing so, after all the particles were replaced, the sample maintained the same void ratios under the controlled confining pressure (e.g. void ratio *e* of the consolidated sample was 0.7 at 1 MPa confining pressure). Hydrate particles were then added into the soil samples using the same preparation process as mentioned above. After the sample preparation, a series of properly designed undrained triaxial compression tests were conducted on the consolidated samples with hydrate particles inside the pores.

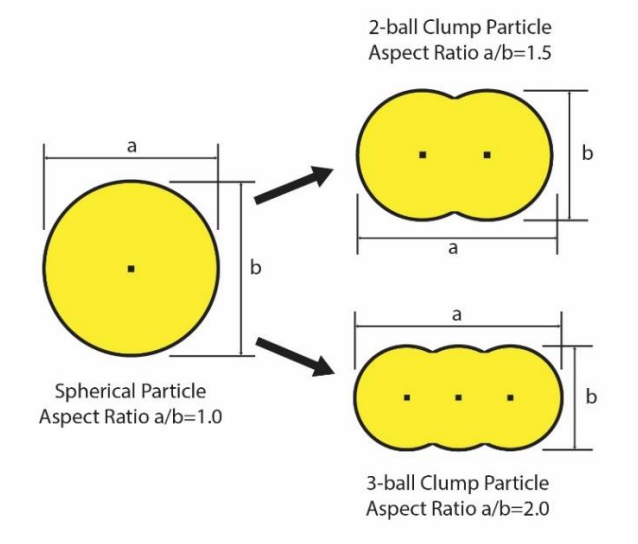

Fig. 3. Replacement of spherical soil particles by elongated clumps.

3 Numerical simulation results

After the sample preparation, a series of drained triaxial compression tests were performed at different hydrate saturations, confining pressures and with hydrate growth patterns in the three different particle shape samples. The analysis was conducted and the comparisons were made.

3.1 Stress-strain responses and stiffness

The stress-strain responses of the spherical soil model under a confining pressure of 1 MPa are illustrated in Fig. 4(a), as a reference. Three different samples are shown: (a) S_h = 0%, (b) pore-filling model with S_h= 40% and (c) cementation model with S_h = 40%. The maximum deviator stress increased with hydrate saturation from 1.37 MPa (S_h=0%) to 2.75 MPa (S_h =40%) in the pore-filling model (by about 100% increase), and from 1.37 MPa (S_h =0%) to 5.50 MPa (S_h =40%) in the cementation model (an increase of almost 300%). There is a hardening effect of hydrate saturation in the case of both hydrate growth patterns. However, for the same amount of increase in the hydrate

saturation, both the elastic stiffness and peak strength of the pore-filling sample were smaller than those of the cementation sample, showing the significant influence of the hydrate growth pattern.

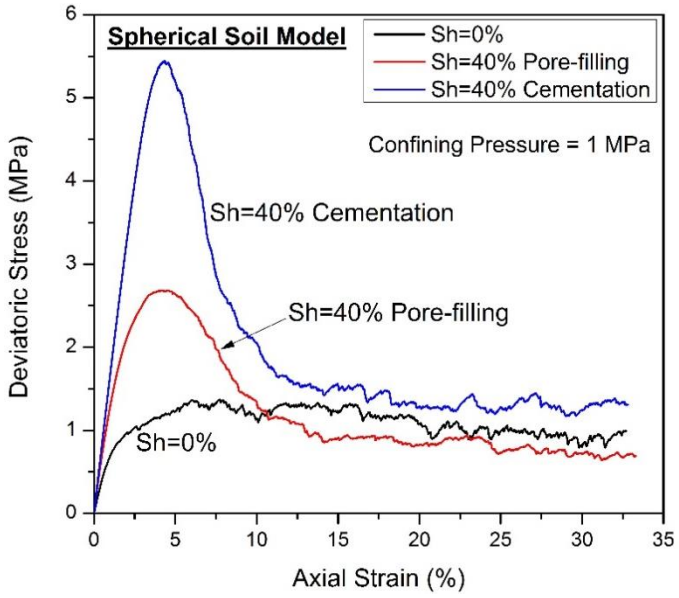

Fig. 4(a). Comparisons of deviatoric stress as a function of axial strain between pore-filling and cementation cases at S_h =40% (Spherical soil model)

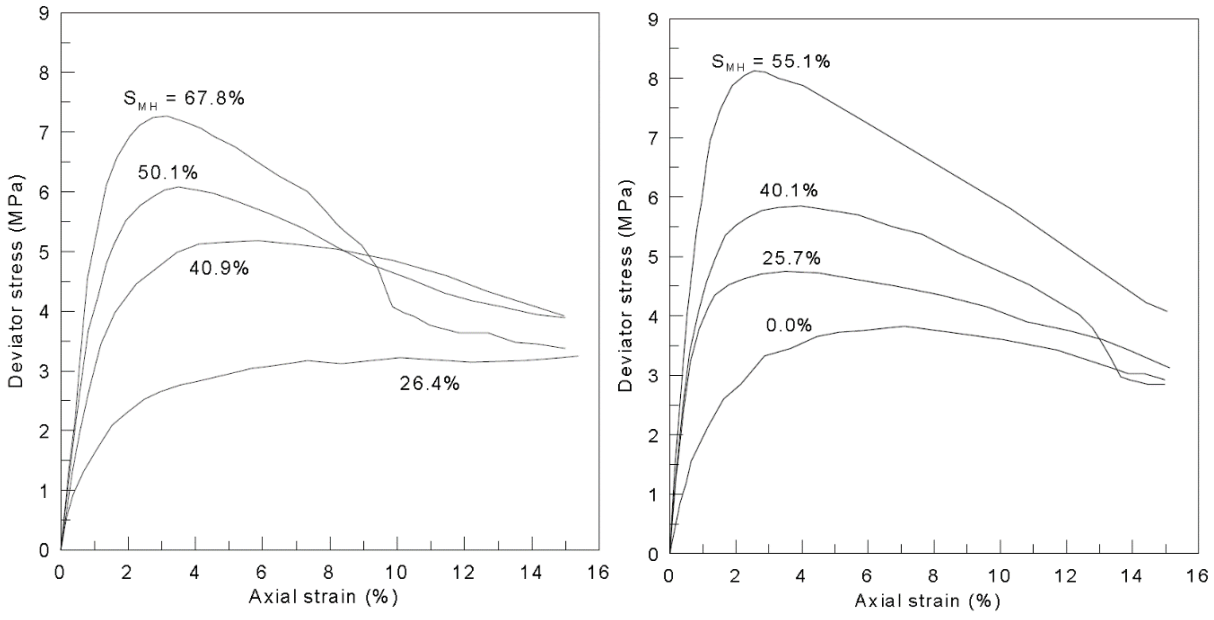

Fig. 4(b). Experimental stress-strain behaviours of Methane hydrate bearing soils with different hydrate saturations: (a) week bond samples; (b) strong bond samples (after Masui *et al*. [12]).

At large strain - critical state, the pore filling model exhibited smaller shear strength (about 20% decrease) than the pure soil sample S_h=0%, as shown in Fig. 4. The cementation model did not show such reduction (it increased by about 20%). In the pore filling model, both soil and hydrate particles moved together at large strain, with the hydrate particles involved in transmitting the main contact forces in the matrix. The much softer hydrate particles in the matrix weakened the overall strength of the system. On the other hand, in the cementation model, it was observed that some hydrate particles kept bonded with the soil particles. This essentially made larger and irregular shaped aggregated particles, which led to greater shear resistance than the sample with spherical particles only.

The experimental data presented by Masui *et al* [12] is shown in Fig. 4(b) for comparison. A strong bond sample (cementation pattern) and a weak bond sample (normally considered as the pore-filling pattern) were prepared by Masui et al. (2005) in their synthetic methane hydrate specimens. The sediment sand is Toyoura sand. The triaxial compression test results under the initial isotropic effective confining stress of 1 MPa for the strong bond samples and the weak bond samples are shown in Figure. The constant shearing rate was 0.1%/min under drained conditions. The peak strength increased with the hydrate saturation. In Figure (a) for the strong bond model, the peak strength increase began even at a low hydrate saturation; while in Figure 4(b) for the weak bond model, the obvious increase in peak strength started from S_h=26.4%. And at the same saturation, the stiffness and peak strength of the strong bond case showed a higher value than those of the weak bond case. In addition, at the large strain, the higher saturation samples of the weak bond case exhibited a lower strength than the relatively lower saturation sample; while the strong bond model did not show

this phenomenon obviously. It is possible that, due to the existing weak bonding between the particles in the weak bond samples, the residual strength of high saturation samples was still larger than the S_h=26.4% sample. Although this observation does not coincide exactly with the characteristics of the DEM pore-filling model, the simulation results are qualitatively comparable behaviour with the experimental data.

Fig. 5(a) shows the stress-strain relationships of three samples of different particle shapes when there is no hydrate. Fig. 5(b) illustrates the degradation of the secant Young's modulus E_{sec} as a function of the axial strain of the three samples. Both stiffness and strength increased with the increase in aspect ratio. The initial stiffness increased dramatically from about 88 MPa in the sphererical soil sample to 216 MPa in the 3-ball clump soil sample, an increase of around 145%. Peak strength increased by about 100% from the sphere soil sample to the 3-ball clump soil sample. The critical state strength increased with the increase in aspect ratio as well (by about 100%).

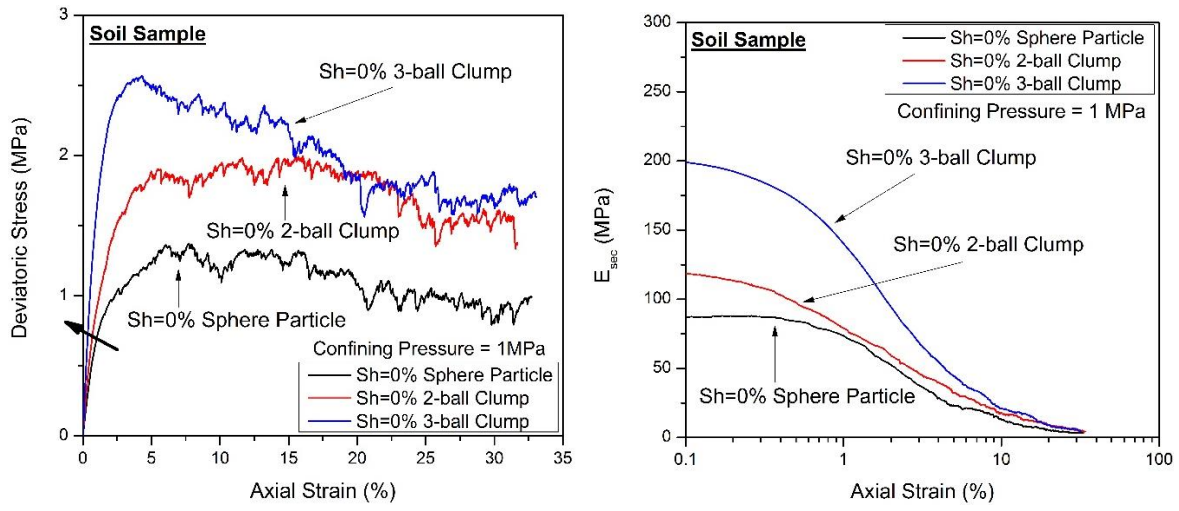

(a) Deviatoric stress (b) Degradation of secant Young's modulus

Fig. 5. Deviatoric stress and degradation of secant Young's modulus as a function of axial strain of three soil models (S_h=0%)

Fig. 6 shows the stress-strain relationships of different hydrate saturation samples for a given particle shape (Fig. 6a for 2 ball clamp and Fig. 6b for 3 ball clamp). Results suggest that the hydrate-bearing samples with elongated particles exhibited a similar trend in the mechanical response to the samples with spherical particles, as shown in Fig. 4 at the peak state. Fig. 7 shows the effect of particle shapes on the stress-strain relationships for a given hydrate growth pattern. In both the pore-filling model and the cementation model, the stiffness and peak strength of the hydrate-bearing soil samples (at S_h=40%) only slightly increased with the increasing aspect ratio of the soil particles. This percentage increase was not as evident as the no-hydrate case (see Fig. 5). This was because the hydrate particles in the pores greatly dominated the behaviour at the peak state.

Fig. 7(a) also shows that, when comparing the cases with the same 40% hydrate saturation, the critical state strengths of the pore-filling models with different shaped soil particles were almost the same. This suggests that the soft hydrate particles are totally dominating the behaviour at the critical state, removing all the shape effect of the soil particles. In the cementation model (Fig. 7(b)), on the other hand, the critical state strengths were not the same. This indicates that the soil particles are still contributing to the critical state shear resistance even under the influence of hydrate particles in the cementation samples. As shown in Fig. 6, there is now no obvious increase in the critical state strength with the cementation models when the soil particles became elongated. This revealed two compensating phenomena. When the soft hydrate particles lost the bonded contacts, they were easier

to be involved in the shearing when soil particles were more elongated. However, due to the large number of remaining bonded hydrate particles, the critical state skeleton of the cementation model was still higher than that of the pore-filling model.

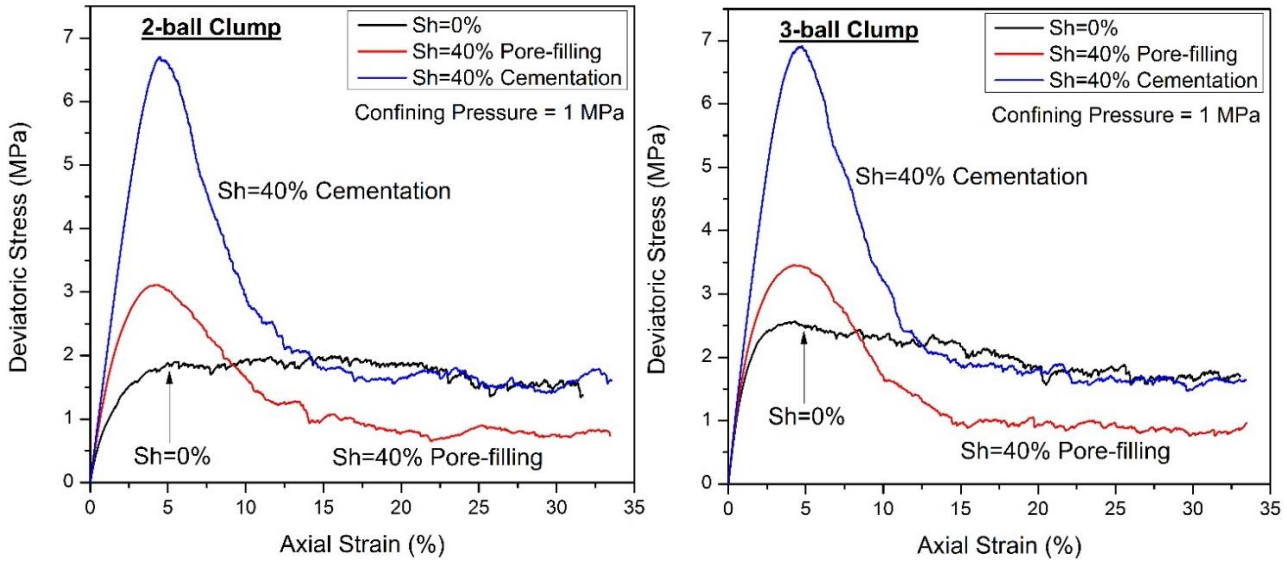

(a) 2-ball clump (aspect ratio 1.5) (b) 3-ball clump (aspect ratio 2.0)

Fig 6. Comparisons of deviatoric stress as a function of axial strain between pore-filling and cementation samples at S_h=40% (elongated soil particles at aspect ratios 1.5 and 2.0)

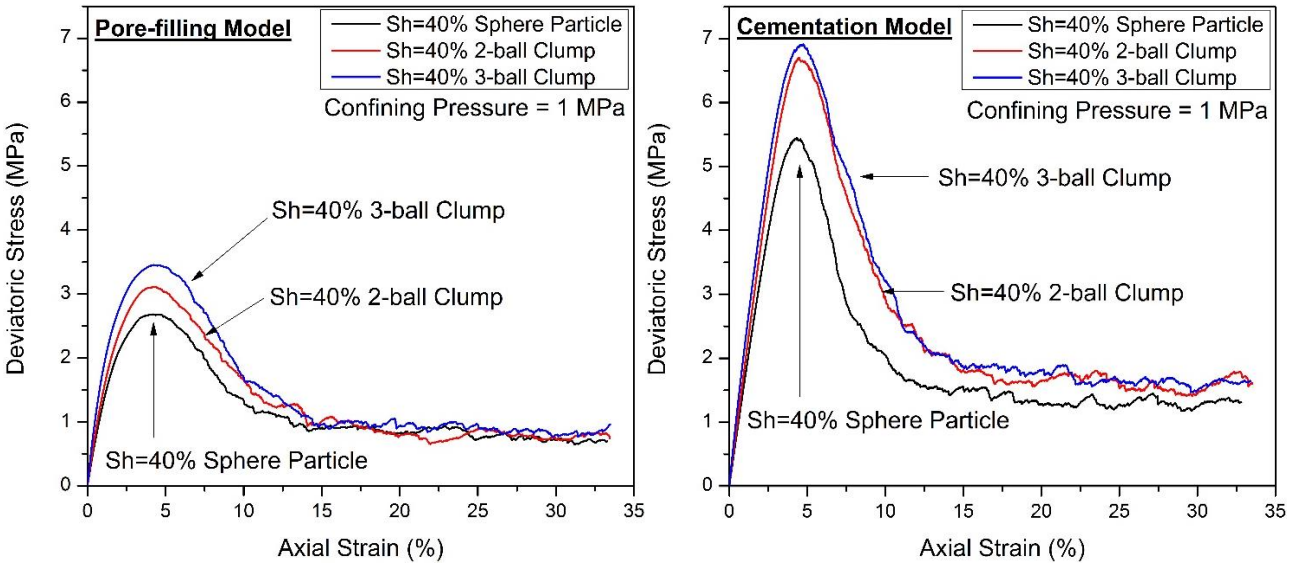

(a) Pore-filling S_h=40% (b) Cementation S_h=40%

Fig. 7. Comparisons of deviatoric stress as a function of axial strain of three soil models at S_h=40%: (a) pore-filling model, (b) cementation model

The degradation curves of secant Young's modulus of the three soil models (S_h = 40%) are plotted in Fig. 8(a) and 8(b). Fig. 8(a) shows that, in the pore-filling samples with elongated soil particles, the increases of the initial stiffness (axial strain = 0.1%) from that of the samples with spherical soil particles were 11% (2-ball clump) and 55% (3-ball clump). Similarly, in the cementation samples as shown in Fig. 8(b), the increases were 12% (2-ball clump) and 59% (3-ball clump). After adding many hydrate particles to the elongated soil particle samples, the extra increase in the stiffness due to the added hydrate particles was not as evident as the increase in stiffness due to a change in the shape of pure soil particles (Fig. 5(b)). Thus, the shape of soil particles had more influence on stiffness than the hydrate saturation. These suggested that: (1) stiffness generally increased with hydrate saturation regardless of the soil particle shape; and (2) the cementation model exhibited a similar effect on stiffness compared to the pore filling model in terms of the initial stiffness at high hydrate saturation (please see Yu *et al*, 2013 for further detail), whereas the shape of the soil particles significantly governed the magnitude of stiffness. Therefore the DEM simulations with elongated hydrate-bearing soil samples compared better to the stiffness values of the synthetic samples in the experimental study of Masui *et al.* [12]. Further research is required to obtain a quantitatively comparable model, for example, on factors such as the input contact stiffness values of the soil particles and of the hydrate particles, or the shape and morphology of the hydrate particles.

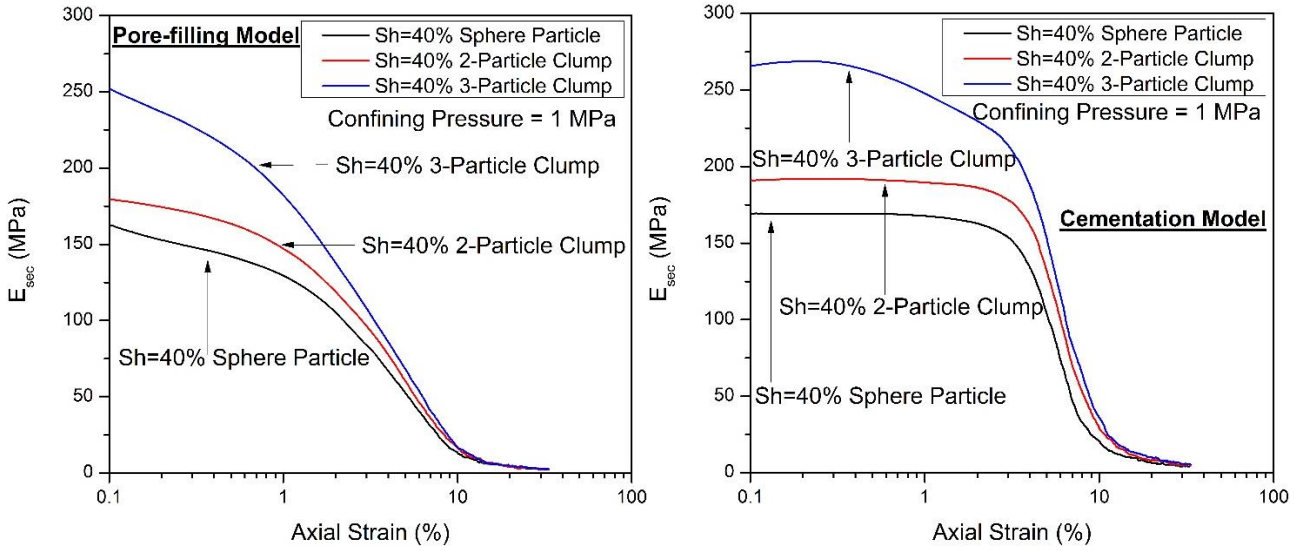

(a) Pore-filling S_h=40% (b) Cementation S_h=40%

Fig. 8. Degradation of secant Young's modulus the three hydrate-bearing soil models (S_h = 40%)

The comparative impact of the three soil particle shape models with two different hydrate growth patterns can be seen more clearly in Fig. 9, as the mid-strain stiffness E_{50} is plotted against various hydrate saturations. Fig. 9 suggests that: (1) The higher aspect ratio of soil particles, the higher the mid-strain stiffness E_{50}, especially when the aspect ratio was 2.0 (around 100% increase); (2) E_{50} increased with hydrate saturation, the rate of stiffness increase was higher when the saturation was higher. This trend of increase were similar regardless of soil particle shapes; (3) at the same hydrate saturation, E_{50} of the cementation model was always higher than that of the pore-filling model. The increase in E_{50} of the pore-filling models became more apparent only when hydrate saturation was higher than 20%, while the increase in the stiffness of the cementation models started to increase immediately with hydrate saturation. But there was an exception when the soil particles had a high aspect ratio of 2.0, where E_{50} of the pore-filling model increased even when the saturation was low.

This might be due to a change in the shape of the pores with elongated soil particles, making it easier for the hydrate particles to contribute to the increase in stiffness even at lower hydrate saturation.

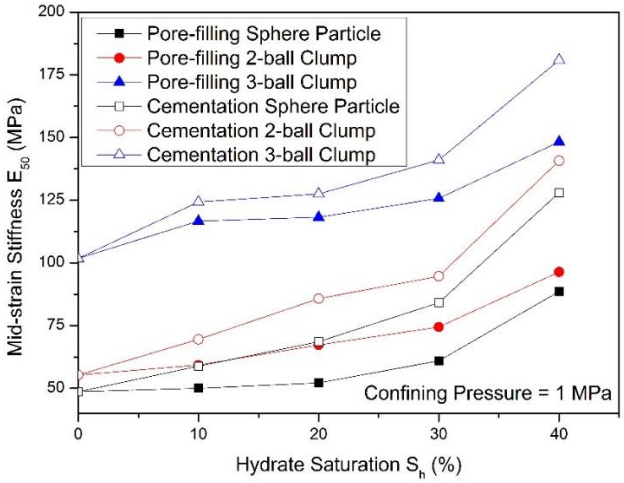

Fig. 9. Mid-strain stiffness E_{50} at various hydrate saturations of three soil particle model

3.2 Strength

The comparative peak strength q_{max} (maximum deviatoric stress) against hydrate saturation was plotted in Fig. 10. The peak strength increased with the aspect ratio in both hydrate-bearing models. As hydrate saturation increased, hydrate particles in the pores played an essential role in shear resistance. As discussed before, the hydrate particles in the pores contributed significantly to the mechanical behaviours. The increased aspect ratio of soil particles did not alter the influence of the hydrate particles, but the hydrate particles did strengthen the matrices of the hydrate-bearing soil samples in a similar manner regardless of the soil particles shape.

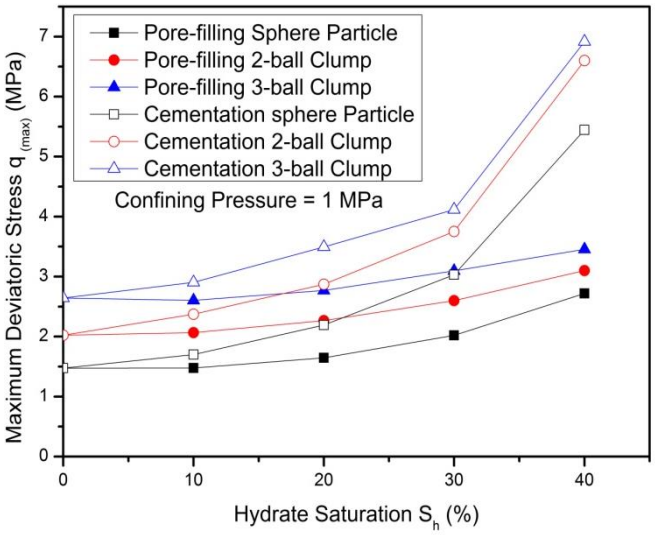

Fig. 10. Peak strength of three soil models

The critical state strength q_{cs} showed a different trend to the peak strength, as shown in Fig. 11. The impact of the compensating effect between the soil particle shape and the pore-filled hydrate particles in the cementation model can be seen more clearly in this comparative Figure. In the pore-filling model, the critical state strength decreased with the increasing hydrate saturation. This was due to the involvement of the softer hydrate particles in the soil matrix at critical state. In the cementation model with a low hydrate saturation of 10%, the critical state strengths were lower than those of hydrate-free soil sediments, and those of the cementation models were always similar to those of the pore-filling models regardless of particle shape. This suggested that most of the inter-particle bonds of the hydrate particles broke, so the hydrate particles moved freely with the soil particles making the system similar to that of the pore-filling cases. However, in the cementation model with a higher hydrate saturation, the critical state strengths increased with hydrate saturation, as there were an increasing number of bonded contacts in the systems. For soil particles with a lower aspect ratio, the cementation effect was more dominant at the highest hydrate saturation. For soil particle with a

high aspect ratio effect, the critical state strength of the cementation model could still be similar to that of the hydrate-free samples. This implies that it was easier to break the cementation bonding in the elongated samples than in the spherical soil sample. An example of bond breakage data is shown in section 3.5.

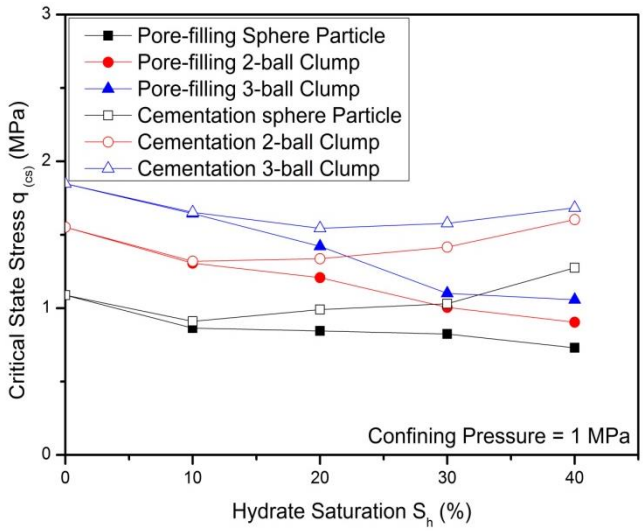

Fig. 11. Critical state strength of three soil models

3.3 Cohesion and friction

The friction angle and cohesion of samples with a given hydrate saturation could be obtained by plotting the failure envelopes for the triaxial simulations under various confining pressures from 1-3 MPa (see Yu, 2015). The cohesion values obtained from the failure envelopes were plotted against the hydrate saturations of the three soil models in Fig. 12, and the friction angles (slope of the envelope) were plotted against the hydrate saturation in Fig. 13.

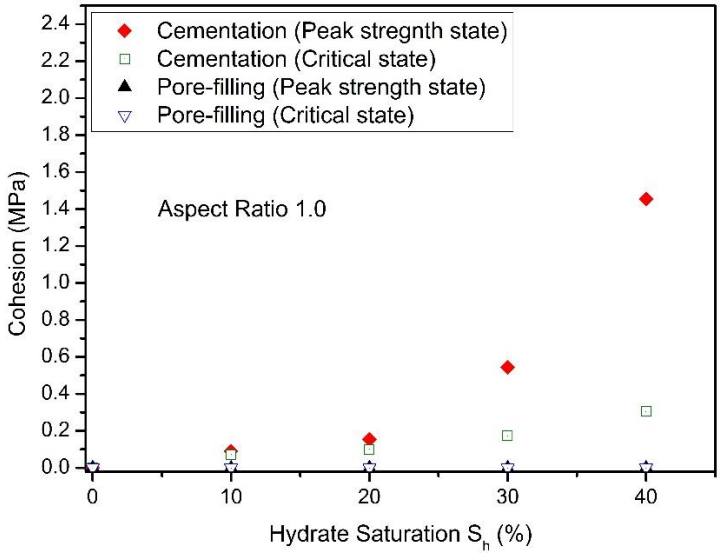

(a) Aspect Ratio 1.0

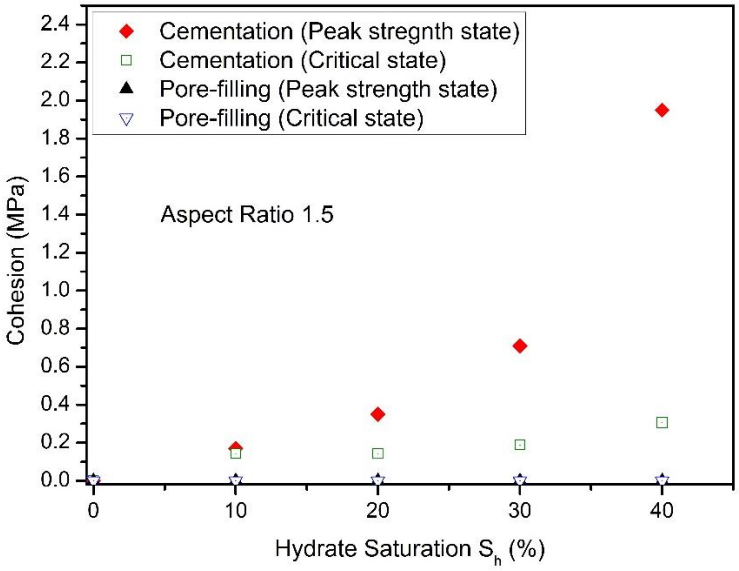

(b) Aspect Ratio 1.5

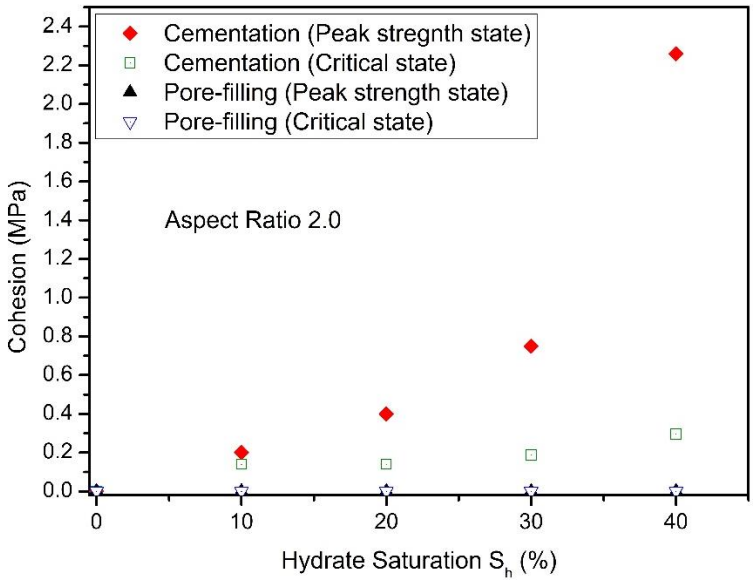

(c) Aspect Ratio 2.0

Fig. 12. Cohesions of three soil models

Firstly, it is found (in Fig. 12) that, by comparing the pore-filling model and the cementation model, the only contribution to the increase in the cohesion was the bonding between hydrates and other particles (hydrates and soils). Thus, the cohesion values were zero for all the cases of the pore-filling model. Secondly, due to the increasing amount of bond breakage during shearing, the cohesion at the peak state was always higher than that of the critical state in the cementation model, which was more significant at a higher saturation. Thirdly, at the same saturation, the peak state cohesion increased as the soil particles were more elongated; however, the aspect ratio of the soil particles did not change the critical state cohesion. In order to reduce from a higher peak cohesion to a similar critical state cohesion, there must be more breakage of the cementation bonding to samples with higher soil aspect ratio. This is consistent with the physical explanation given in the previous section.

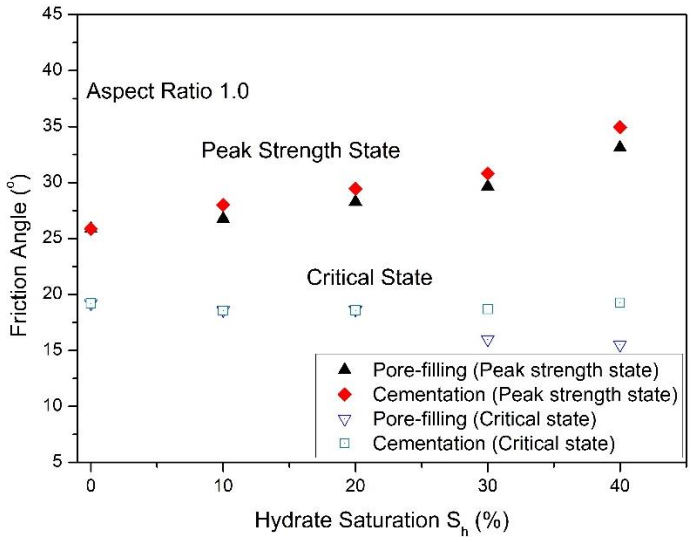

(a) Aspect Ratio 1.0

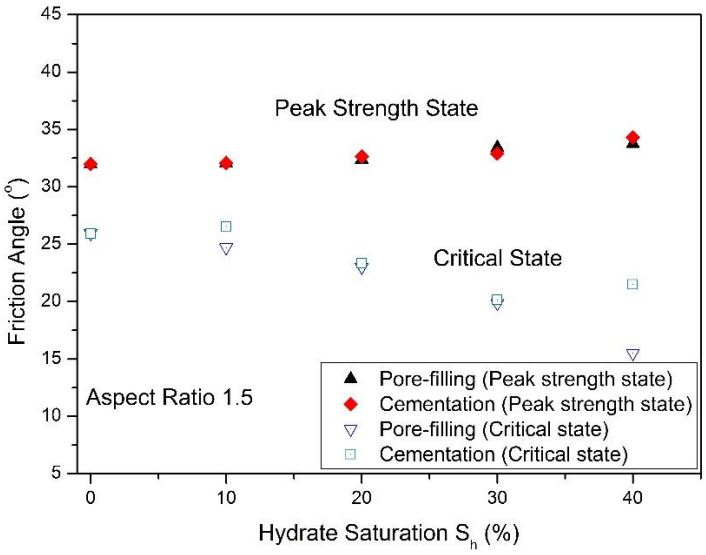

(b) Aspect Ratio 1.5

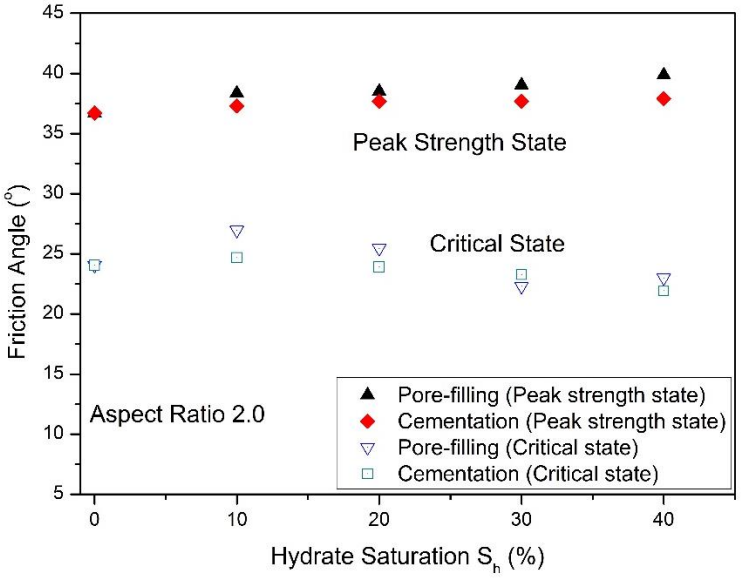

(c) Aspect Ratio 2.0

Fig. 13. Angles of friction of three soil models

Fig. 13 shows that the peak friction angle of the S_h=0% sample evidently increases with the aspect ratio. However, as the aspect ratio increased, the increase in the friction angles with hydrate saturation became less obvious. When the aspect ratio was 1.0, the peak friction angle of the cementation model was larger than that of the pore-filling model. However, when the aspect ratio was 1.5, the friction angle of the cementation model was similar to that of the pore-filling model. In addition, when the aspect ratio was 2.0, the friction angle of the cementation model was slightly smaller than that of the pore-filling model. All these are due to the cohesion development which resulted in a lower apparent friction. This is similar to the observation given by Waite *et al.* (2009) stating that friction angle is largely independent of hydrate saturation. Hence, the simulation results

with elongated soil particles reproduced a closer match to the mechanical response of the natural sediments. The critical states frictions however showed similar trends as the critical state strength.

3.4 Volumetric responses

Under the confining pressure of 1 MPa, the volumetric strain against axial strain relationships are illustrated in Fig. 14. Fig. 14(a) shows the volumetric responses of spherical soil models: (1) S_h = 0%, (2) pore-filling model with S_h= 40% and (3) cementation model with S_h = 40%, corresponding to the stress-strain responses shown in Fig. 4(a). The sediments initially showed elastic contractive behaviour then followed by a dilation. The peak contractive value in the pore-filling model were similar to that in the pure soil sample, whereas that in the cementation model was larger due to a large number of bonding contacts with the soft hydrate particles. When particles started to move relative to one another, dilation happened. Both pore-filling and cementation hydrates caused a larger dilation compared to the pure soil sample. The rate of dilation of the cementation model was greater than that of the pore filling model, meaning cementation enhanced dilation. The volumetric responses of the three hydrate-free soil samples, corresponding to the data shown in Fig. 5, are illustrated in Fig. 14(b). The rate of dilatancy increases with soil elongation. The increased dilatancy rate also extended to higher axial strain when the soil particles were elongated, resulting in a higher critical state volume.

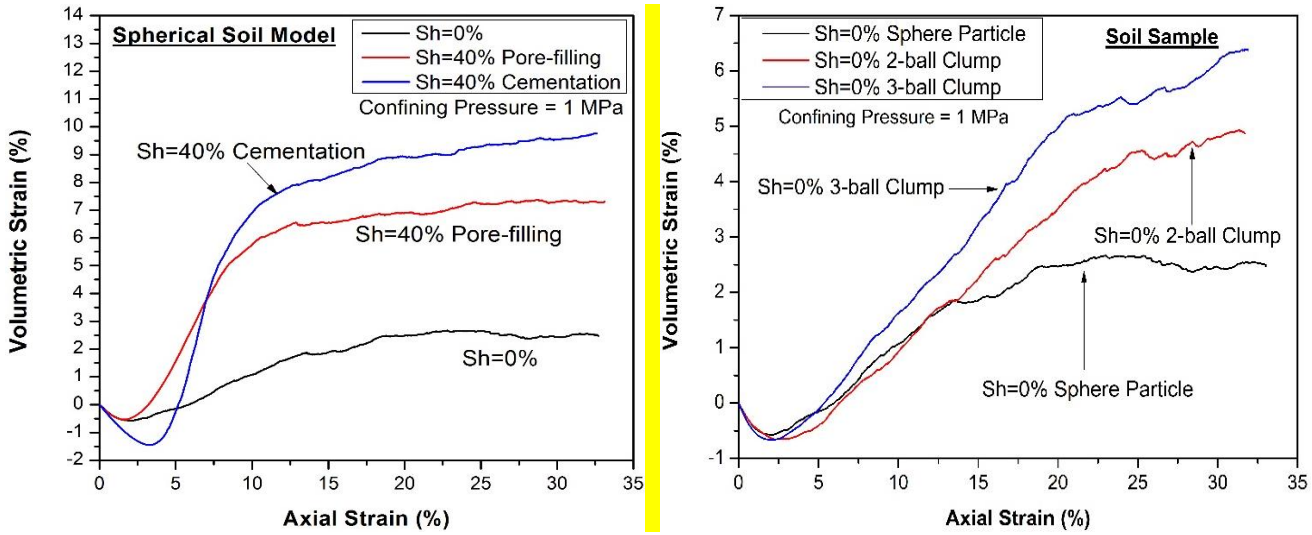

(a) Spherical soil model (b) Three kinds of soil models

Fig. 14. Volumetric response volumetric strain as a function of axial strain: (a) spherical soil model; (b) three kinds of soil models (S_h =0%)

Fig. 15 shows that the increase in the hydrate saturation enhanced the dilative characteristics of the hydrate-bearing sediments, and the increase was more obvious when the saturation was higher. However, unlike the hydrate-free soil models (Fig. 14), the angle of dilation of the hydrate-bearing samples with elongated soil particles (especially with very high hydrate saturation) was lower than that of the samples with spherical soil particles. This implies that shearing of samples with elongated soil particles triggers more bonding breakage than those with spherical soil samples. In addition, for the pore-filling model, the angles of dilation for the cases with hydrate saturation higher than 10% were very similar, showing a relatively insignificant impact of the soil particle shape in this model. These findings suggest again that the dilation was affected by several factors including (1) the hydrate saturation, (2) the cementation bonds between particles, and (3) the soil particle shape. Hydrate

saturation effect in the pore-filling cases are more dominant than the particle shape effect. The particle shape effect is more apparent to the cementation model especially when the hydrate saturation is high.

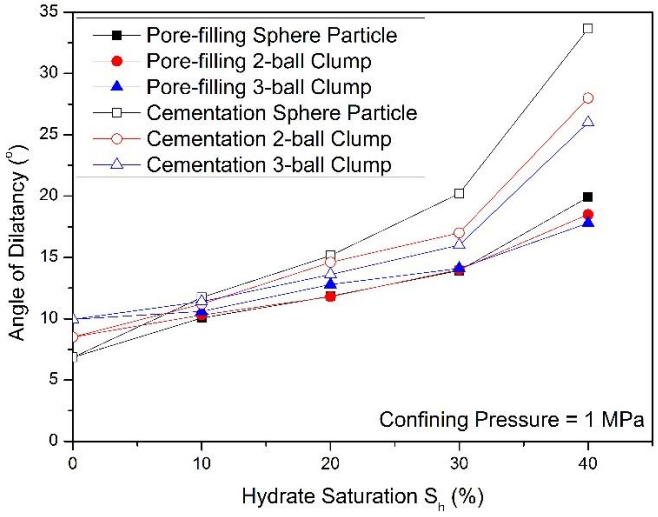

Fig. 15. Dilation angle as a function of hydrate saturation at different aspect ratios

The critical state granular void ratio $e - \ln p'$ projections were plotted in Fig. 16. The granular void ratio is defined as the void ratio of the pores created by the soil particles after the hydrate particles are removed. It can be seen that, in both pore-filling and cementation models, the critical state granular void ratios of the elongated soil models were larger than those seen in the spherical soil model. In all the three soil models, the hydrate effects on dilation produced higher critical state void ratios as the saturation increased. It is also suggested that the hydrate-induced dilatancy was less evident at a high confining pressure. As the confining pressure increased, the dilation characteristic tended to diminish in the pore-filling model. The dilation behaviour was also weakened by the confining pressure in the cementation model, although due to the remaining unbroken bonds it could not be similar to the pore-filling cases.

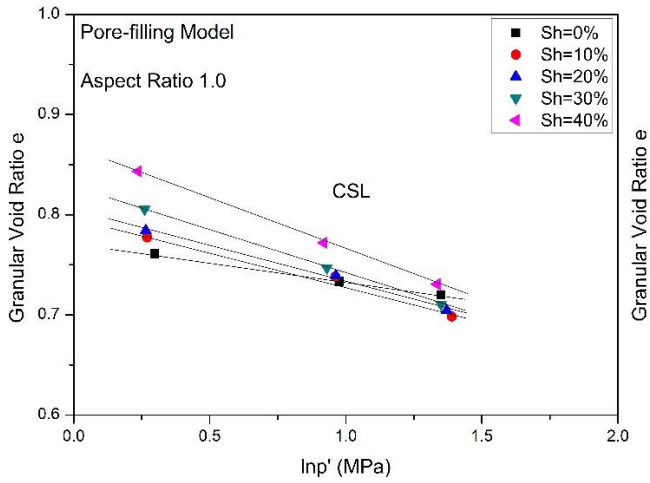

(a) Pore-filling Aspect Ratio 1.0

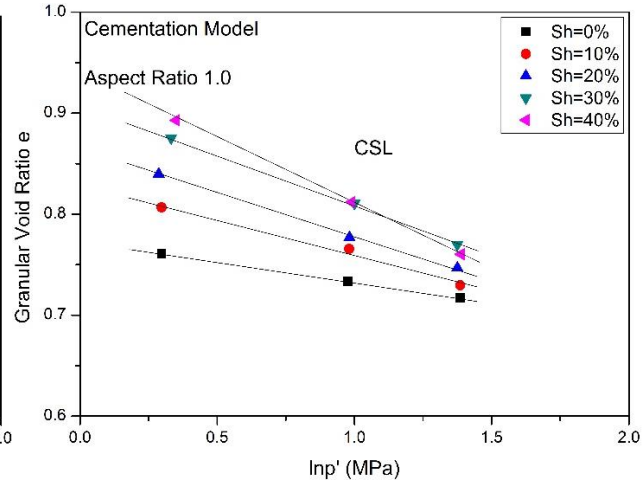

(b) Cementation Aspect Ratio 1.0

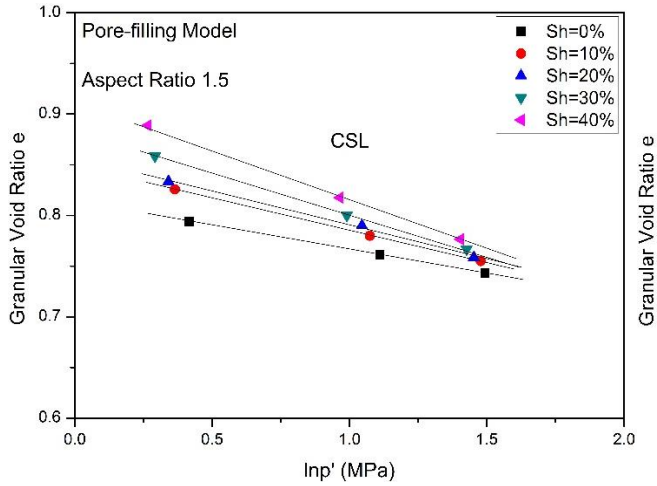

(c) Pore-filling Aspect Ratio 1.5

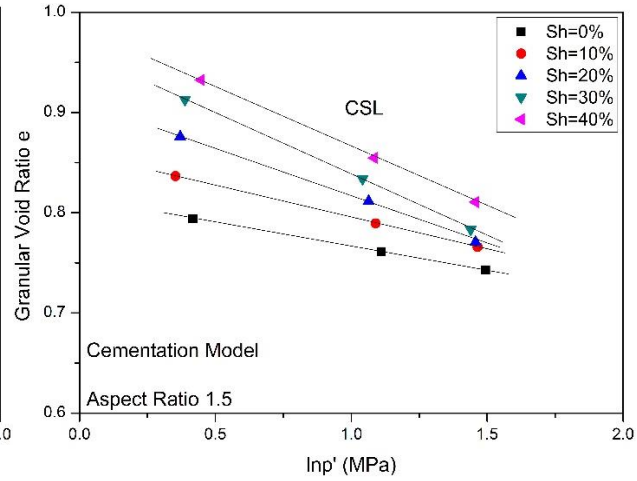

(d) Cementation Aspect Ratio 1.5

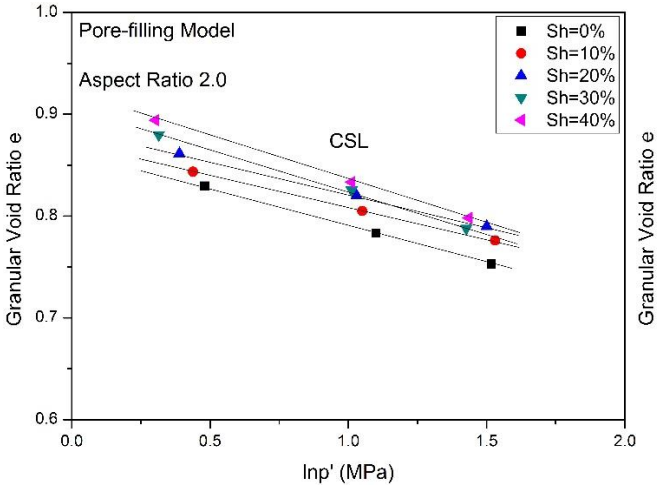

(e) Pore-filling Aspect Ratio 2.0

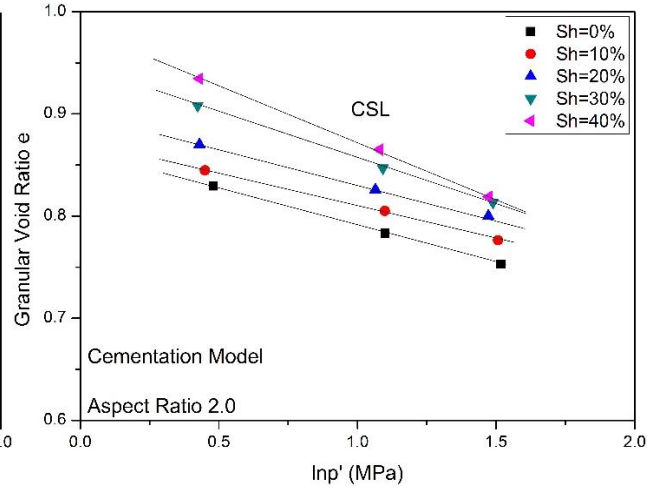

(f) Cementation Aspect Ratio 2.0

Fig. 16. Critical State Line projection on Granular Void Ratio $e - \ln p'$ plane

3.5 Bond Breakage

Since the macroscopic data implies that shearing of samples with elongated soil particles potentially triggers more bonding breakage than those with spherical soil samples. Hence, an example of breakage data is shown in Fig. 17, which consists of a comparison between the spherical soil sample and the elongated soil samples at S_h=30%. This is a typical saturation with relatively high number of hydrate particles' bonding contacts, but allowing the freed hydrate particles to move in the pore space. Although the number of the contact bond breakage was very small in the initial state, it was evident that bond breakage began to happen just after the elastic phase, and the percentage of bond breakage in total bonds increased steadily. The percentages of bond breakage of the elongated soil samples were evidently larger than that of the spherical soil sample.

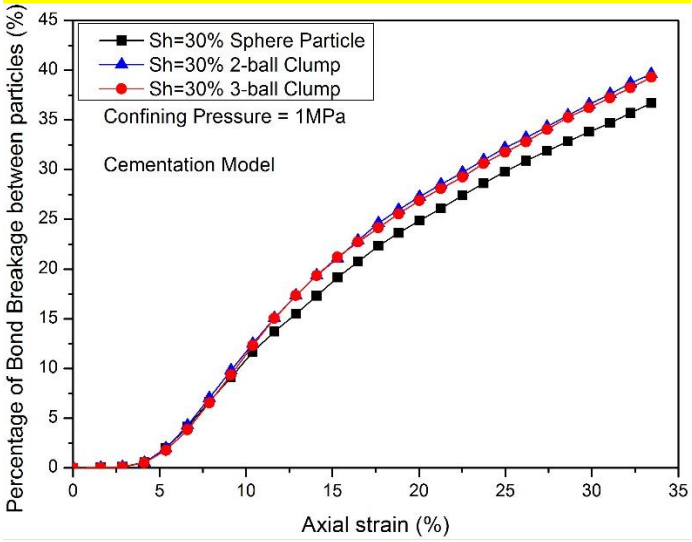

Fig. 17. Bond Breakage in the triaxial test of cementation model at S_h=30%

4 Discussions

The abovementioned sections have illustrated that the macroscopic mechanical behaviour of methane hydrate sediments is highly dependent on hydrate distribution patterns, soil particle shape and hydrate saturation, from the initial state, peak state and towards to the critical state. With the elongated soil particles, the overall mechanical behaviour was found to be much closer to the experimental results with real methane hydrate sediments. Fundamentally, the elongated soil particles could form a more complex microstructure providing a higher shearing resistance and experience a more complicated microstructure evolution process, comparing to the one with sphere soil particles. The overall stress tensor can be decomposed into a number of contact-type related stress tensors, as well as the deviatoric stress [26]. For the methane hydrate bearing soils, there are three contact-type related contributions from: (1) the soil-soil (s-s) contacts; (2) the hydrate-soil (h-s) contacts, and (3) the hydrate-hydrate (h-h) contacts. Herein, we attempted to study the micromechanics of different characteristics of deviatoric stress evolutions, as shown in Fig. 10 and Fig. 11, by investigating these contact-type related contributions.

Fig. 18 and Fig. 19 present the contact-type related contributions to the peak deviatoric stress ($q_{\max}$) and the deviatoric stress at critical state (q_{cs}), respectively, for both porefilling and cementation cases with sphere soil particles. The results show that the contributions of three-type contacts to the overall mechanical behaviour of hydrate bearing sediments depend largely on its growth pattern and the trend observed in the peak strength is different from that in the critical state strength. At the peak state, Fig. 18(a) shows that, for the pore-filling model, the contribution from all three types of contact increase with the increasing of hydrate saturation. For example, the

contributions from s-s, h-s and h-h contacts are 1.591MPa, 0.041MPa and 4.697E-5MPa at 20% hydrate saturation, and 2.290MPa, 0.316MPa and 0.019MPa at 40% hydrate saturation, respectively. In the cementation case, there is a similar, yet much stronger increasing trend, as shown in Fig. 18(b). The contributions from s-s, h-s and h-h contacts are 2.012MPa, 0.120MPa and 0.002MPa at 20% hydrate saturation, and 4.291MPa, 0.689MPa and 0.086MPa at 40% hydrate saturation, respectively. Interestingly, for both pore-filling and cementation cases, the combined contributions from h-h and h-s contacts remain in a relative low levels, with the maximum values of 0.335MPa and 0.775MPa at $S_h = 40\%$, respectively. This implies that the increases of $q_{\max}$ in both models are mainly due to the enhancement of the interaction between soil-soil particles, rather than the hydrate bonding effect.

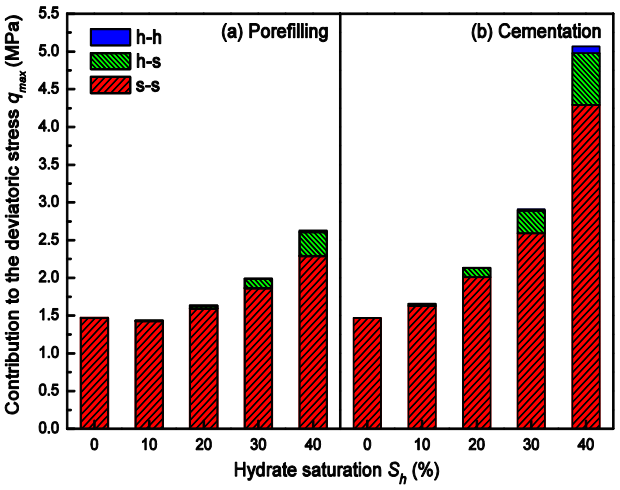

Fig. 18. Contribution of three-type contacts to the peak deviatoric stress

At the critical state of the pore-filling model, as shown in Fig. 19(a), the contributions from the s-s contacts reduce significantly when hydrate saturation increases. At 20% and 40% hydrate saturations, contributions from s-s, h-s and h-h contacts are 0.751MPa, 0.057MPa and 8.580E-5MPa, and 0.493MPa, 0.198MPa and 0.002MPa, respectively. These show that, at large deformation, the

existence of a larger number of softer hydrate particles significantly reduced the contribution of the s-s contacts, which is the major contribution to the deviatoric stress. For the cementation case, the contributions from the s-s contacts remain approximately constantly, with 0.809MPa at 20% hydrate saturation and 0.914MPa at 40% hydrate saturation, respectively.

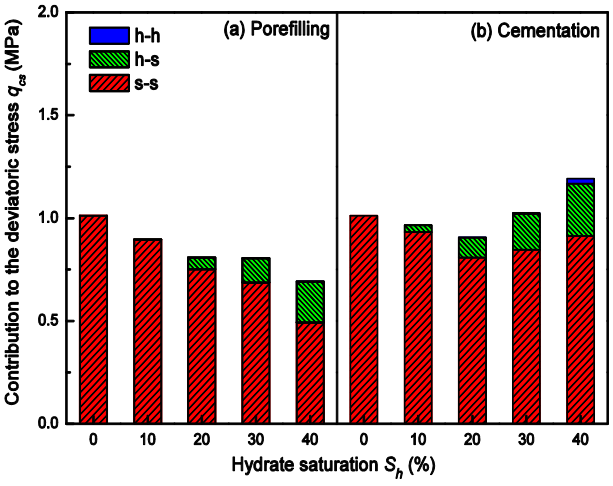

Fig. 19. Contribution of three-type contacts to the deviatoric stress at critical state

Fig.s 20-23 present the effect of soil particle shape on $q_{\max}$ and q_{cs} for both porefilling and cementation cases. For the pore-filling cases with elongated soil particles, as shown in Fig. 20, the contribution of s-s contacts to $q_{\max}$ remains approximately the same as the hydrate saturation increases, when comparing the same soil particle shape model. At 0% hydrate saturation, the contribution of s-s contacts to $q_{\max}$ increases significantly with the increasing of soil particle aspect ratio, with 1.469MPa, 2.048MPa and 2.887MPa for sphere particle, 2-ball clump and 3-ball clump models, respectively. However, at 40% hydrate saturation, the effect of soil particle shape becomes less pronounced, with 2.290MPa, 2.363MPa and 3.068MPa for sphere particle, 2-ball clump and 3-ball clump models, respectively. The steady increasing in $q_{\max}$ with hydrate saturation is purely

due to the added contributions from the h-s and h-h contacts, with 0.335MPa, 0.582MPa and 0.692MPa for sphere particle, 2-ball clump and 3-ball clump models (S_h=40%), respectively. For the cementation case, as plotted in Fig. 21, the contribution of s-s contacts to $q_{\max}$ increases significantly as the hydrate saturation increases for all three cases with different soil particle shape. However, the effect of soil particle shape on s-s contribution becomes less remarkable when the hydrate saturation increases. For example, the s-s contributions for sphere particle, 2-ball clump and 3-ball clump models are 2.012MPa, 2.377MPa and 3.218MPa at 20% hydrate saturation, and 4.291MPa, 4.270MPa and 5.304MPa at 40% hydrate saturation, respectively.

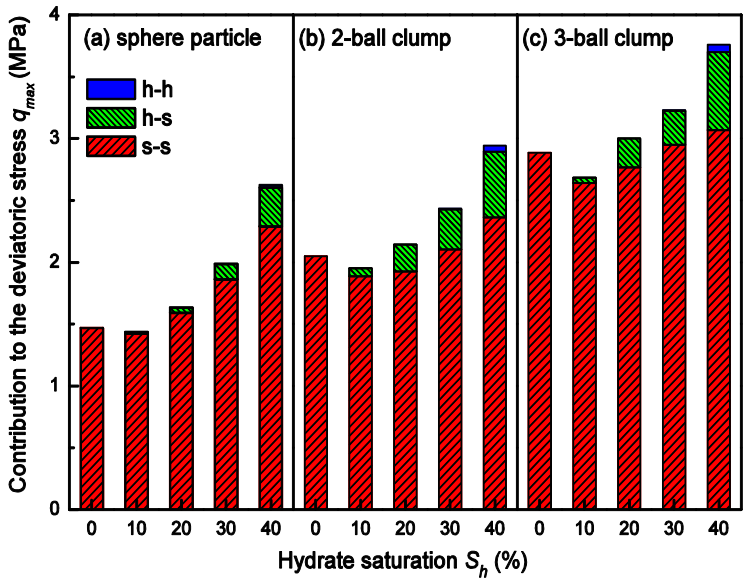

Fig. 20. Particle shape effect on the peak deviatoric stress (pore-filling case)

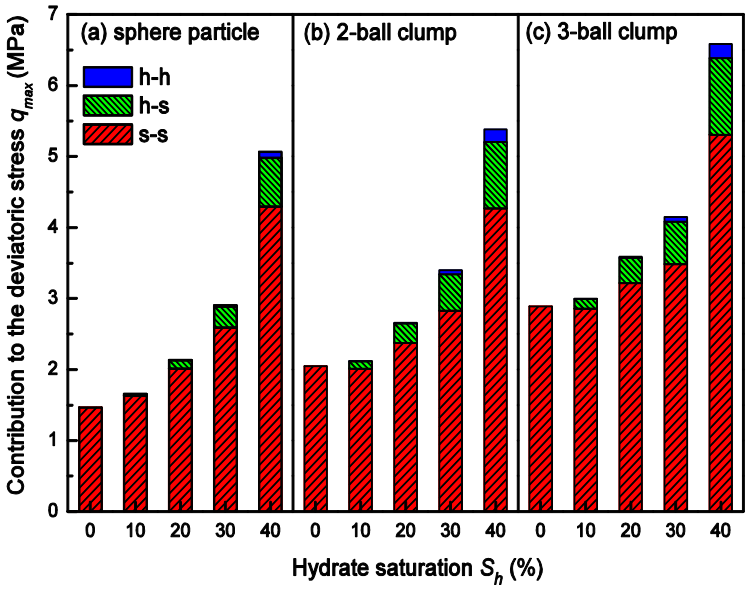

Fig. 21. Particle shape effect on the peak deviatoric stress (cementation case)

Fig. 22 and Fig. 23 show the effect of particle shape on the deviatoric stress at critical state. For both pore-filling and cementation cases, the s-s contact contribution to q_{cs} decreases with the increase of hydrate saturation. The higher soil particle aspect ratio, the greater the reduction. For instance, in the pore-filling case, the contributions from the s-s contacts at the critical state reduce from 1.012MPa, 1.613MPa and 2.113 at 0% hydrate saturation, to 0.514MPa, 0.536MPa and 0.698MPa at 40% hydrate saturation for sphere particle, 2-ball clump and 3-ball clump models, respectively, as shown in Fig. 22. Interestingly, the latter is much lower than the ones in the cementation models, as shown in Fig. 23, with 0.893MPa, 0.912MPa and 1.088MPa, respectively. These indicate that, at large deformation, the existence of a larger number softer hydrate particle in the cementation model plays a better role in preserving the soil particle structure than that in the pore-filling model.

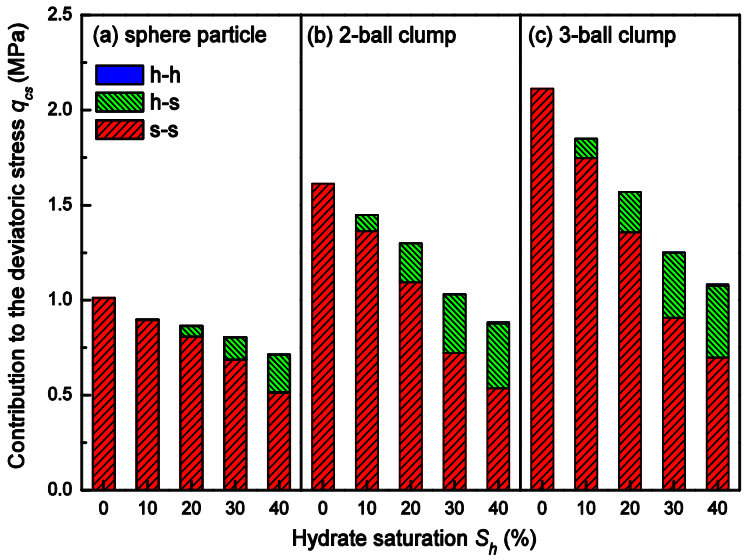

Fig. 22. Particle shape effect on the critical state deviatoric stress (pore-filling case)

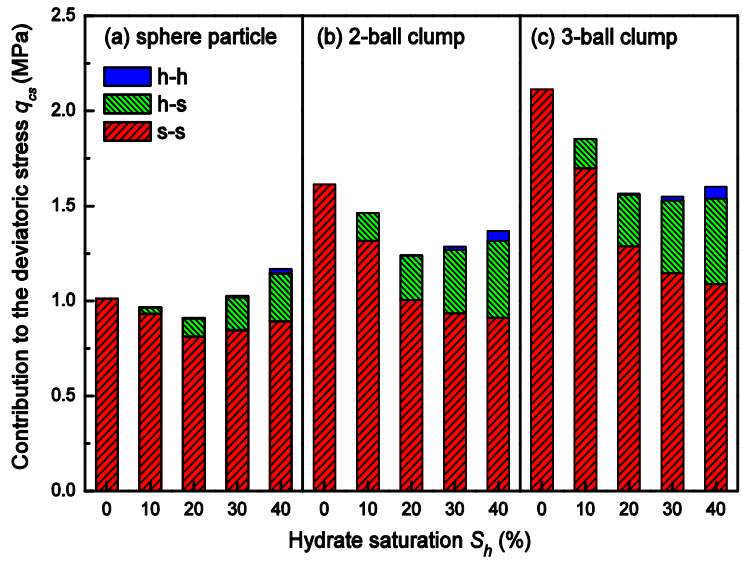

Fig. 23. Particle shape effect on the critical state deviatoric stress (cementation case)

The results show that the contributions of hydrates to the overall mechanical behaviour of hydrate bearing sediments depend largely on its growth pattern and the trend observed in the peak strength is different from that in the critical state strength. For the peak strength, hydrates gives pure additional strength increment to the original soil strength (soil-soil contact) in the pore filling case. In the cementation case, however, the presence of hydrates not only adds strength by its hydrate-soil

contact, but also enhances the existing soil strength (soil-soil contact), magnifying the effect of hydrates on the peak strength. This is because the shape of hydrate bonded soil particles become irregular and bigger, which leads to increase in dilatancy and peak strength.

At the critical state, many hydrate particles move around the soil voids by large deformation and start to interact more directly to soil particles. In the pore filling case, the presence of hydrates makes its critical strength to decrease because free moving small hydrate particles move in between large soil particles by large deformation and their soft nature contributes to the overall strength. In the cementation case, however, the effect of hydrates is more complex. The detached hydrate particles make the soil softer as discussed before. But the shape of the hydrate bonded soil particles also becomes irregular and they are aggregated, making the soil stronger. The two compensating effects create complex strength variation with hydrate saturation as shown in Fig.s 21 and 23. In this study, the hydrates are modelled as small particles. In reality, they can disintegrate into even smaller particles by shearing. Hence, further work is needed to understand the contribution of hydrates and their disintegration as shearing continues.

5 Conclusions

In this paper, the Discrete Element Method (DEM) was employed to provide some insights into the macro- and micro- mechanical behaviour of hydrate-bearing sediments with two different hydrate distribution patterns: pore-filling and cementation. The soil particles were modelled separately using spherical particles or elongated clumps with two different aspect ratios, in order to investigate the influence of the soil particle shape effect on the mechanical behaviour of hydrate-bearing sediments. A series of drained triaxial compression tests were performed to study the effects of soil particle shape, hydrate saturation (S_h) and hydrate growth.

The effect of soil particle shape on the overall mechanical behaviour of hydrate sediments was found to be significant. Although the trends on increasing stiffness and strength with hydrate saturation were similar among different particle shapes, the magnitudes of stiffness and strength were greater in samples with elongate soil particles than in those with spherical particles. The values obtained from elongated soil particles gave closer match to the experimental results reported by Masui *et al.* (2005).

The hydrates not only strengthened the sediments' skeleton in the initial and peak states, but also induced the softening behavior in the critical state as the softer hydrates moved into the soil matrix. Meanwhile, the hydrate growth patterns greatly influenced the hydrate-bearing soil sediments. For the pore-filling models, the soft hydrate particles totally dominated the behaviour of the critical state, removing all the shape effect of the soil particles. The cementation hydrate particles induced larger

stiffness and strength than the pore-filling hydrates. However the shape of the soil particles was still contributing to the critical state strength given the great influence of the hydrate particles. This is due to the two contrasting phenomena. When the soft hydrate particles lost the bonded contacts, it was easier for them to be involved in the shearing when soil particles were more elongated. However, due to the large number of remaining bonded hydrate particles, the critical state skeleton of the cementation model was still higher than that of the pore-filling model. In general, the hydrate saturation effect in the pore-filling cases were more dominant than the particle shape effect, whereas the particle shape effect was more apparent to the cementation model especially when the hydrate saturation was high.

Acknowledgement

This research work was conducted under the collaboration between University College London (UCL) and University of Cambridge during the period from 2010 to 2014. The first author would like to thank the Ministry of Education of China, the UK Government Department for Business, Innovation and Skills (BIS) and University College London (UCL), for the UK-China Scholarships for Excellence and all their other generous financial supports.

Reference

[1] Soga, K. & Lee, S.L. & Ng, M.Y.A. & Klar, A. 2006. Characterisation and engineering properties of methane hydrate soils. Characterisation and Engineering Properties of Natural Soils, Taylor and Francis, Vol. 4, pp.2591-2642.

[2] Waite, W. F. & Santamarina, J. C. & Cortes, D. D. & Dugan, B., et al. 2009. Physical properties of hydrate-bearing soils. Rev. Geophys, 47(RG4), 3－41.

[3] Helgerud, M. B., Dvorkin J., Nur A., Sakai A., and Collett T. (1999). Elastic-wave velocity in marine sediments with gas hydrates: Effective medium modeling, Geophys. Res. Lett., 26, 2021–2024, doi:10.1029/1999GL900421.

[4] Dvorkin, J., Prasad M., Sakai A., and Lavoie D. (1999). Elasticity of marine sediments: Rock physics modeling, Geophys. Res. Lett., 26, 1781–1784, doi:10.1029/1999GL900332.

[5] Clayton, C. R. I., Priest, J. A. & Best, A. I. (2005). The effects of disseminated methane hydrate on the dynamic stiffness and damping of a sand. Geotechnique 55(6), 423–434.

[6] Clayton, C. R. I., Priest, J. A. and Rees, E. V. L. (2010). The effects of hydrate cement on the stiffness of some sands. Geotechnique 60(6), 435–445.

[7] Priest J. A. & Best A. I. & Clayton C. R. I. 2005. A laboratory investigation into the seismic velocities of methane gas hydrate-bearing sand, Journal of Geophysical Research, 2005, vol. 110, doi: 10.1029/2004JB003259

[8] Priest, J. A., Rees, E. V. L., and Clayton, C. R. I. (2009), Influence of gas hydrate morphology on the seismic velocities of sands, J. Geophys. Res., 114, B11205, doi:10.1029/2009JB006284.

[9] Santamarina, J. C. and Ruppel, C. (2008). The impact of hydrate saturation on the mechanical, electrical, and thermal properties of hydrate-bearing sand, silts, and clay. In: The 6th International Conference on Gas Hydrates. Vancouver, Canada.

[10] Yun, T. S., Lee, C., Lee, J.-S., Bahk, J. J. and Santamarina, J. C. (2011). A pressure core based characterization of hydrate-bearing sediments in the Ulleung Basin, Sea of Japan (East Sea). Journal of Geophysical Research 116(B2), 1–12.

[11] Hyodo, M. & Yoneda, J. & Nakata, Y. & Yoshimoto, N. 2011. Strength and dissociation property of methane hydrate bearing sand. Proceedings of the 7th International Conference on Gas Hydrates (ICGH2011), Edinburgh, Scotland, United Kingdom, July 17-21, 2011.

[12] Masui, A. & Haneda, H. & Ogata, Y. & Aoki, K. 2005. The effect of saturation degree of methane hydrate on the shear strength of synthetic methane hydrate sediments. Proceedings of the 5th Int. Conf. on Gas Hydrates. June 13-16, Trondheim, Norway. Paper No. 2037.

[13] Cheng, Y. P., Nakata, Y., Bolton, M. D., (2003). Discrete element simulation of crushable soil. Geotechnique, 53, No. 7, 633-641.

[14] Itasca 2008, PFC3D: Particle flow code. User's guide version 4.0, Minneapolis, USA.

[15] Brugada, J. & Cheng, Y. P. & Soga, K. & Santamarina, J. C. 2010. Discrete element modelling of geomechanical behaviour of methane hydrate soils with pore-filling hydrate distribution, Granular Matter, vol. 12, no. 5, pp. 517-525.

[16] Yu, Y. & Cheng, Y. P. & Soga, K. 2012. Mechanical behaviour of methane hydrate soil sediments using Discrete Element Method: Pore-filling hydrate distribution. The proceedings of the International Symposium on Discrete Element Modelling of Particulate Media, Birmingham, RSC Publishing, March 2012, pp. 264-270.

[17] Yu, Y. & Cheng, Y. P. & Xu, X. & Soga, K. 2014. DEM study on the mechanical behaviours of methane hydrate sediments: hydrate growth patterns and hydrate bonding strength, Proceedings of the 8th International Conference on Gas Hydrates (ICGH8-2014), Beijing, China, 28 July - 1 August, 2014.

[18] Yu, Y. & Xu, X. & Cheng, Y. P. & Soga, K. 2013. Study on small-strain behaviours of methane hydrate sandy sediments using discrete element method, Powders and Grains 2013, AIP Conf. Proc. 1542, 555-558 (2013), doi: 10.1063/1.4811991.

[19] Jiang, M. J. & Sun, Y. G. & Yang, Q. J. 2013. A simple distinct element modelling of the mechanical behaviour of me-thane hydrate-bearing sediments in deep seabed, Granular Matter, 15: 209-220, doi: 10.1007/s10035-013-0399-7.

[20] Jung, J.W & Santamarina, J.C. & Soga, K. 2012. Stress-strain response of hydrate-bearing sands: numerical study using DEM simulations, Journal of Geophysical Research - Solid Earth, Vol. 117, B04202, 12 pp., doi:10.1029/2011JB009040

[21] Jo, S.A. & Kim, E.K. & Cho, G.C. & Lee, S.W. (2011). Particle shape and crusing effects on direct shear behaviour using DEM. Soils and Foundations, Vol. 51, No. 4, 701-712, Aug. 2011, Japanese Geotechnical Society.

[22] Santamarina, J.C. and Cho, G.C. (2004). Soil behaviour: the role of particle shape. Proceedings of Skempton Conference, March, London

[23] Kezdi, A. (1974). Handbook of Soil Mechanics. Elsevier, Amsterdam.

[24] Prat, M., Bisch, E., Millard, A., Mestat, P., and Cabot, G. (1995). La modelisation des ouvrages. Hermes, Paris.

[25] Yu, Y. 2015. Micromechanical investigation of hydrate-bearing sediments with Discrete Element Method. PhD thesis, University College London.

[26] Minh, N. H. & Cheng, Y. P. 2014. Strong force networks in granular mixtures. Granular Matter, 16 (1), 69－78.

[27] M. Jiang, F. Zhu, F. Liu, and S. Utili, "A bond contact model for methane hydrate-bearing sediments with interparticle cementation," *Int. J. Numer. Anal. Methods Geomech.*, vol. 38, pp. 1823–1854, 2014.